

WAVE NUMBER-BASED CRITERION FOR DYNAMIC MESH REFINEMENT IN CFD

Patrick H. Reisenthel[‡] and Robert E. Childs[¶]

Nielsen Engineering & Research, Inc.
Mountain View, CA

ABSTRACT

Three local spectral estimation schemes were compared for their ability to accurately detect the presence of excess energy in high frequency modes lying outside the accuracy bandwidth of a given discretization scheme: the windowed Fast Fourier Transform (FFT), the Discrete Wavelet Transform (DWT), and the Maximum Entropy Method (MEM). Systematic deterministic and statistical tests were carried out, indicating the MEM to be the most accurate. An MEM-based on-the-fly grid refinement / derefinement scheme was developed. Its capabilities are demonstrated in terms of local grid refinement, local grid coarsening, and dynamic adaptation.

NOMENCLATURE

A_i	Input Amplitude
A_o	Output Amplitude
A_o/A_i	Amplitude transfer function
c	Airfoil chord
DWT	Discrete wavelet transform
e	Internal energy
FFT	Fast Fourier transform
fv	Finite volume
m	Number of points in data record
M	Mach number
MC	Macrocell
MEM	Maximum entropy method
opt	Optimized
p	Pressure
PDF	Probability density function
Q	Solution vector
r	Radius
Re	Reynolds number ($Re = U_\infty c/\nu$)
$S(\omega)$	Power spectral density
t	Time
u	Streamwise velocity

U_∞	Freestream velocity
UMC	Unstructured MacroCell
v	Normal velocity
v_θ	Tangential velocity
w	Spanwise velocity
x	Streamwise coordinate
y	Normal coordinate
z	Spanwise coordinate
Γ	Circulation
Δx	Grid spacing
λ	Wavelength
ρ	Fluid density
ω	Angular frequency
ω_c	Energy cutoff frequency
ω_F	Filter cutoff frequency
ω^*	Bandwidth of numerical scheme
Ω	Vorticity
ν	Kinematic viscosity
ξ_x	Grid stretching parameter
$\%E_{>\omega}$	Percentage energy above ω_c
\sim	On the order of
$\langle \cdot \rangle$	Mean

1. MOTIVATION AND BACKGROUND

Although the need for a high quality driver for grid enrichment exists in a number of computational disciplines, the primary motivation behind this study was the development of an advanced adaptive computational fluid dynamics (CFD) methodology for predicting the phenomenon of dynamic stall.

A number of studies in recent years (for example, Ref. 1) have focussed on the proposition that the genesis of dynamic stall is associated with an extremely thin vorticity spike which forms within the unsteady leading edge boundary layer. This possibility has driven the needs of Eulerian-based CFD methods towards ever greater mesh

[‡] Chief Scientist, Member AIAA

[¶] Executive Vice-President, Member AIAA

refinement levels (Refs. 2,3). Using present CFD methods and computers, the highest achievable chord Reynolds number is estimated to be around $Re = 100,000$ (Ref. 2), a factor of 40 from what is needed for full-scale rotorcraft simulations. Converged calculations of an impulsively started dynamic stall problem have been carried out (Ref. 3) up to Reynolds numbers of 800,000. However, achieving this result required a combination of extreme grid clustering and a very high-accuracy (8th-order) CFD algorithm.

These facts led to the belief that full-scale Navier-Stokes simulations of dynamic stall might be achievable in two dimensions, provided the computational prediction tool incorporates both adaptive mesh refinement and high-accuracy algorithms. Achieving these two properties *simultaneously* and *efficiently* was the basis for the development of a new CFD methodology, the Unstructured MacroCell (UMC) method (Ref. 4).

The UMC concept (Ref. 5) utilizes a nested structure consisting of coarse unstructured “macrocells” and, within each macrocell, a fine structured grid. The unstructured nature of the grid at the macrocell level gives the method geometric flexibility, while the element of structure, at the microcell level, allows the use of high-accuracy algorithms.

While a good dynamic adaptive solver is an essential aspect of an accurate CFD method for dynamic stall, its ultimate success hinges on the development of mesh enrichment indicators which enable the grid refinement to “stay ahead” of a nonlinear solution which is generating finer and finer scales.

Grid refinement indicators typically rely on gradient-like quantities of the type $D\rho/Dt$ or $\nabla\rho$. Such indicators are inappropriate for the onset of dynamical stall, which manifests itself with initially *weak high-frequency* vortical flow features (for instance, the occurrence of a subboundary layer scale vorticity spike). Low-order CFD methods are unable to pick up these initially low-energy, high-wave number phenomena and, hence, subsequent grid refinement may never occur.

2. OBJECTIVE

For a given spatial discretization scheme, numerical error can be identified by the presence of energy in high frequency modes lying outside the accuracy bandwidth of the discretization scheme (**Figure 1**). The objective of this study was to evaluate practical criteria for on-the-fly spectral error estimation. The connection between gradients and high frequency is imprecise, as steep straight lines are resolved perfectly by even a first-order scheme. The goal, therefore, is to find a method which is wave number-based, allowing the accurate detection of energy outside the accuracy bandwidth of the CFD algorithm. By considering

the local spectral content of the solution and its grid metrics, sharp grid refinement / derefinement indicators can be developed based on sound scientific principles.

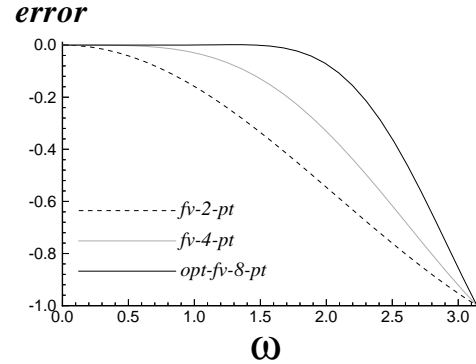


Fig. 1. Discretization Error Versus Wave Number for Two- and Four-Point Finite-Volume Taylor Series, and Eight-Point Optimized Approximations of the Convective Fluxes, from Reference 6.

3. METHOD

To solve the Euler or Navier-Stokes equations on a curvilinear grid, the governing equations are subjected to a generalized coordinate transformation from physical space (x,y,z,t) to computational space (ξ,η,ζ,τ) . Due to the transformation, the flow equations

$$\frac{\partial Q}{\partial \tau} + \frac{\partial E}{\partial x} + \frac{\partial F}{\partial y} + \frac{\partial G}{\partial z} = 0$$

are modified by numerous grid metric terms and may be rewritten as

$$\frac{\partial \bar{Q}}{\partial \tau} + \frac{\partial \bar{E}}{\partial \xi} + \frac{\partial \bar{F}}{\partial \eta} + \frac{\partial \bar{G}}{\partial \zeta} = 0$$

where the contravariant quantities \bar{Q} , \bar{E} , \bar{F} , \bar{G} are defined as

$$\begin{aligned} \bar{Q} &= Q / J \\ \bar{E} &= (\xi_t Q + \xi_x E + \xi_y F + \xi_z G) / J \\ \bar{F} &= (\eta_t Q + \eta_x E + \eta_y F + \eta_z G) / J \\ \bar{G} &= (\zeta_t Q + \zeta_x E + \zeta_y F + \zeta_z G) / J \end{aligned}$$

and J is the Jacobian of the metric transformation.

The basic idea is that a numerical solution on a grid is spatially well-resolved if all of the energy in the contravariant fluxes is within a frequency band $0 \leq \omega \leq \omega^*$. This frequency band must be associated with the wave numbers which are accurately resolved by the given numerical scheme. For example, **Figure 1** shows

how an optimized eight-point finite-volume scheme is accurate up to almost half of the resolvable wave number range ($\omega_{\text{Nyquist}} = \pi$). By contrast, a fourth-order scheme accurately resolves only approximately 20% of that range. This number drops to less than 3% for a conventional second-order scheme.

Note that \bar{E} , \bar{F} and \bar{G} are made of multiplicative terms containing both the fluxes and the grid metrics. It may be shown, therefore, that the bandwidth ω^* is the *sum* of the bandwidth of the metrics and the bandwidth of the solution fluxes. For the present purpose, we are interested in detecting the presence of energy in the high frequency modes of \bar{E} , \bar{F} and \bar{G} , consistent with the spectral characteristics of the discretization scheme being used.

The focus of the methods described below is the evaluation of *local* spectral characteristics based on local (i.e., short) data records. The objective is to produce a measure which can be used for subsequent grid refinement / coarsening.

The first method that was considered is the Fast Fourier Transform (FFT). The advantages of this method are that the errors associated with FFT are well-understood and a number of efficient algorithms have been developed. The main difficulty with the Fourier transform is its poor spectral definition when there are limited amounts of data. The underlying assumption of stationarity of the input signal requires that periodic windowing functions be used. The performance of the FFT was documented and compared for five different types of windowing functions (rectangular (implicit), Hanning, Hamming, Bartlett, and Welch). In all cases, the spectral estimates (even for monochromatic data) are broadband once the size of the input of data stencil is less than 20.

The Maximum Entropy Method (MEM) of spectral analysis, on the other hand, produces sharply defined peaks from as little as five data points. The development of the MEM is attributed to Burg (Ref. 7). Entropy, in the information theory sense, is a measure of unpredictability (noise) in a given process. Concepts of maximization of the information entropy, consistent with the measured lags of the autocorrelation function can be used to produce a minimum phase inversion filter which maximizes the amount of "self information." The MEM was first developed in the fields of astrophysics and geophysics (Ref. 8), where it proved to be a powerful tool, particularly in cases where very limited amounts of data are available. A comparison of MEM and FFT spectra for a truncated monochromatic signal is shown in **Figure 2**.

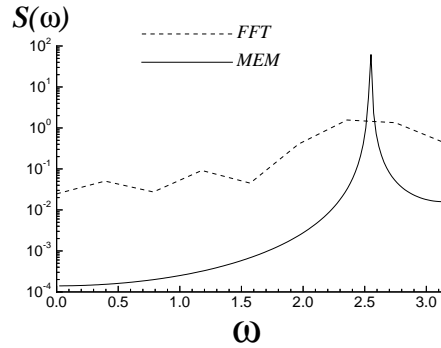


Fig. 2. Power Spectral Density of a Fifteen-Point Truncated Sinusoid Computed by FFT and MEM.

The third method that was investigated in this study is the Discrete Wavelet Transform (DWT). Like the FFT, the DWT can be thought of as an efficient algorithm to decompose an input signal onto a basis of orthogonal functions. In the case of the FFT, the basis functions are sines and cosines. In the case of the DWT, they are functions with compact (finite) support referred to as wavelets. The wavelet transform has received much attention in the past decade, mostly because of its ability to represent signals in a compressed form. Thus, it has been the basis for numerous data compression algorithms, and even new solution algorithms for large linear systems of equations (Ref. 9). In the present study, two classical sets of wavelet filter coefficients were used. These filter coefficients are referred to as Daubechies-4 and Daubechies-20.

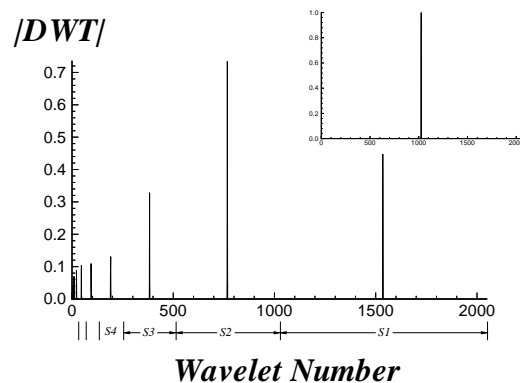


Fig. 3. Discrete Wavelet Transform of a Pulse Using Daubechies-4 Wavelets.

To illustrate how the method works, consider the example of **Figure 3**. In this example, the input signal (2048 points shown in the inset) is a single short pulse. The output of the DWT is divided into binary segments (top segment: 1025 through 2048, next segment: 513 through 1024, next

segment: 257 through 512, and so on). The top segment corresponds to the finest scales (i.e., no decimation of the input signal), while consecutive segments to the left are associated with successive decimations of the input signal by a factor of two each time. Note that in each segment, the response is compact (unlike the Fourier transform of a pulse, which is broadband) and localized (like the data itself). Within each segment, the pulse-like response may be thought of as a mirroring of the original pulse, viewed through the filter of self-similar wavelets of various scales.

In order to reduce the output data and to be able to compare the DWT results against FFT and MEM, the following operations were performed: (1) the peak response in each segment is recorded (i.e., we are not interested in localization), and (2) each segment is assigned an equivalent "frequency." Based on the pulse analogy, the finest scale segment is assigned the Nyquist frequency, $\omega = \pi$, the next segment is assigned the frequency $\omega = \pi/2$, the next one $\omega = \pi/4$, and so forth.

4. SPECTRAL ESTIMATION RESULTS

By analyzing the power spectral estimates of truncated sinusoids and pulse functions computed using the FFT, MEM, and DWT methods, the following observations were made.

The main problem associated with the FFT is the excessive "leakage" from one frequency bin to the next when dealing with small data records. The windowing operations are designed to minimize this well-known phenomenon. However, they are still inadequate for the extreme conditions being considered here (on the order of 10 data points or less). By contrast, the MEM spectra tend to have sharply delineated peaks and have arbitrarily fine resolution. These are valuable qualities for discrete spectra. On the other hand, the peaky nature of the MEM spectra may lead to unrealistic estimates for processes which are broadband in nature. Whether a spectrum based on a few points should be discrete or broadband is an academic question. In fact, the very meaning of a frequency spectrum under these conditions is unclear. It is, perhaps, easiest to think of these operations (FFT/MEM/DWT) as *filters*. Each of these filters has its own characteristics. Which characteristics are most useful for the purpose at hand is what must be assessed.

Recall that we are interested in estimating locally the amount of energy contained in wave numbers which exceed the bandwidth of the particular spatial discretization scheme being used. Assuming the discretization scheme to be accurate up to $\omega = \omega^*$, a measure of the error is

$$\%E_{>\omega} = \frac{\int_{\omega^*}^{\pi} S(\omega) d\omega}{\int_0^{\pi} S(\omega) d\omega}$$

where $S(\omega)$ is the power spectral density. Alternate measures can also be introduced very simply by weighing the power spectral density based on the accuracy curve of the discretization scheme (see, e.g., **Figure 1**). Examples of $\%E_{>\omega}$ calculated by the three methods on a single data stencil are given in **Figures 4** and **5**.

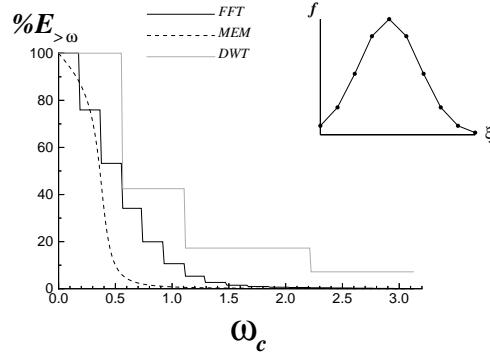


Fig. 4. Percent Energy Above ω_c , Calculated Based on FFT, MEM, and DWT Spectral Estimates. (The input signal is a 10-point pulse shown in the inset.)

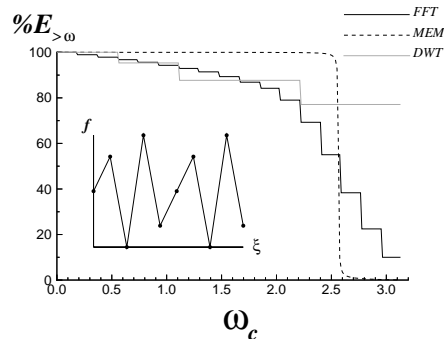


Fig. 5. Percent Energy Above ω_c , Calculated Based on FFT, MEM, and DWT Spectral Estimates. (The input signal is the 10-point truncated sinusoid shown in the inset.)

For a given cutoff frequency ω_c (typically chosen to be equal to ω^*), widely different values of the error are obtained, depending on the method used for spectral estimation. In order to answer the question "Which method is best suited for local error estimation?" one should, ideally, know what the true spectrum is. As previously mentioned, for short data records there is no exact answer against which to compare. Thus, an alternate methodology must be used.

The basic idea behind the alternate testing methodology is to compare the *statistical* properties of $\%E_{>\omega}$ against the true spectrum, obtained from long data records. Consider, for instance, a data record that is sufficiently long, so that its statistical and spectral properties are known with good precision. If the same data record is now segmented into small independent stencils (say, on the order of 10 points), the values of $\%E_{>\omega}$ from spectral estimates based on each individual stencil will follow a certain probability distribution. **Figure 6**, for instance, depicts the normalized Probability Density Functions (PDF) of $\%E_{>\omega}$ for the FFT, MEM, and DWT methods, in the case of filtered white noise (spectrum shown in the inset).

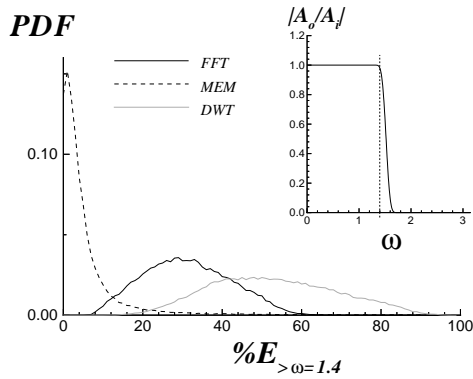


Fig. 6. Probability Density Distributions of the Percentage of Energy Above $\omega_c = 1.4$. (Asymptotic long record spectrum shown in the inset.)

The PDFs plotted in **Figure 6** represent the probability distribution for the percentage of energy above $\omega_c = 1.4$. This probability is obtained from the analysis of 50,000 short ($m = 11$ points) data records. The expected value of $\%E_{>\omega}$ (in the asymptotic limit of a long, continuous record) is obtained from the integral from 1.4 to π of the curve shown in the inset: $\%E_{>\omega} \approx 7.1\%$. For comparison, the averages obtained from the PDFs are: $\langle \%E_{>\omega} \rangle_{\text{FFT}} \approx 31.9\%$, $\langle \%E_{>\omega} \rangle_{\text{MEM}} \approx 5.9\%$, and $\langle \%E_{>\omega} \rangle_{\text{DWT}} \approx 52.9\%$.

Tests like the one depicted in **Figure 6** have been repeated for many input signals and with various integration cutoff frequencies ω_c . Typical results are shown in **Figure 7**. The curve labeled "exact" corresponds to the asymptotic expected value of $\%E_{>\omega}$. Note that, in comparing $\langle \%E_{>\omega} \rangle_{\text{FFT}}$, $\langle \%E_{>\omega} \rangle_{\text{MEM}}$, and $\langle \%E_{>\omega} \rangle_{\text{DWT}}$ to $\%E_{>\omega}$, an implicit assumption is made that the average value obtained from the short data records should tend towards $\%E_{>\omega}$. This is an imperfect assumption at low frequencies, since low frequencies are not represented in the short data records. However, for the high frequencies (say, $\omega > 2\pi/m$) this assumption ought to be valid. By making this assumption, the results of our tests indicate that the Maximum Entropy Method is the closest to being statistically correct.

Since the ideal filter (FFT, MEM, or DWT) is one that must sharply discriminate the presence of spectral energy around a given frequency (typically equal to the accuracy bandwidth, ω^*), the Discrete Wavelet Transform appears to be too coarse a tool in practice. Also, because of frequency leakage, the FFT-based results are inaccurate. The most promising method, therefore, is a filter based on MEM spectral estimation.

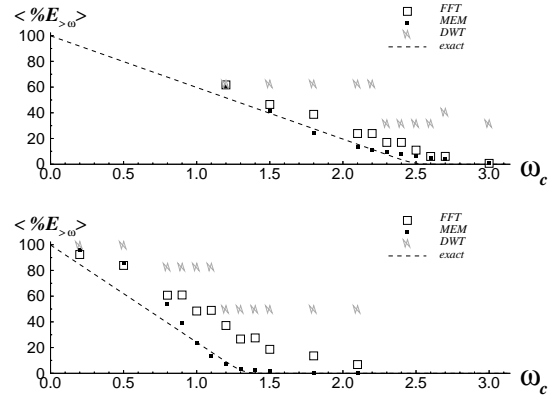


Fig. 7. Average Percentage of Energy Above ω_c , Based on FFT, MEM, and DWT Methods. (Input data is made of 11-point stencils of a low-pass filtered random process; filter frequencies: $\omega_F = 2.3$ (top) and $\omega_F = 1.3$ (bottom).)

Note on the Use of Artificial Dissipation

Before proceeding with documenting the performance of MEM filtering on known fluid dynamical problems, however, one must consider how this method will be used. For a given discretization scheme, the spectral accuracy can be determined very precisely (see, e.g., **Figure 1**). Without grid adaptation, the appearance of energy outside the accuracy band $0 \leq \omega \leq \omega^*$ is usually suppressed through the use of artificial dissipation. For instance, Childs (Ref. 6) has shown how high-order artificial dissipation schemes could be carefully tuned to match the spectral characteristics of a given discretization scheme. The basic idea behind the use of artificial dissipation is to smooth the solution sufficiently, so that its accuracy is consistent with the discretization scheme, given a particular grid. However, in the case where grid adaptation is an option, the appearance of high-frequency energy can be treated in one of two ways. The first is to add artificial dissipation in the manner described above. The second, rather than to *suppress* the high frequencies, is to *refine* the grid so as to *resolve* them, by effectively shifting the energy to lower, accurately resolved frequencies on the new grid. The latter approach is the most accurate for detecting and capturing the formation of gradients within the flow. However, it is not realistic to consider 'doing without' artificial dissipation altogether. Instead, the best approach is to minimize the

amount of artificial dissipation, perhaps tailoring it to kick in at higher frequencies, and use a measure such as $\langle \%E_{>\omega} \rangle_{MEM}$ to drive grid refinement. Whatever the strategy, the artificial dissipation itself may be used as a measure of the error.

An example of the characteristics of a high-order artificial dissipation scheme is given in **Figure 8**. This 10-point scheme is designed to leave the frequencies below ω^* essentially unaltered, and to act on the modes whose frequency exceeds ω^* . The calculation of the artificial dissipation can be regarded as a high-pass filter operation. In the case shown in **Figure 8**, the spectral characteristics of the artificial dissipation scheme closely match those of the error of the discretization scheme. Thus, the artificial dissipation operation can act as an error estimator which weighs energy modes in accordance with the accuracy of the discretization method. This natural measure of the error has certain advantages. Properly normalized, it should be equivalent to a weighted form of $\%E_{>\omega}$. It is also an inexpensive quantity which is or can be computed on-the-fly. As mentioned previously, a detection scheme combining $\langle \%E_{>\omega} \rangle_{MEM}$ and artificial dissipation is a likely candidate as a numerical error estimator. A comparison of their characteristics is described below.

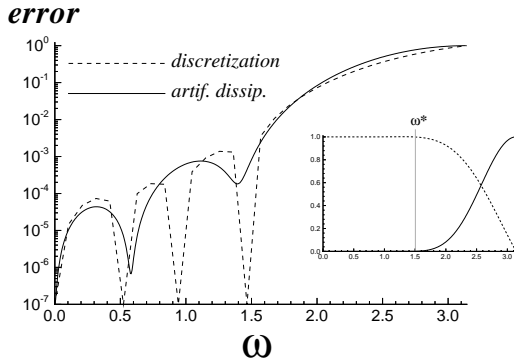


Fig. 8. Superposed Plot of Discretization Error (Optimized Eight-Point Scheme) and Normalized Artificial Dissipation (Optimized Ten-Point Scheme), from Reference 6.

Suppose the spatial discretization scheme being used is the optimized eight-point scheme whose characteristics are depicted in **Figure 8**. The useful bandwidth is: $\omega^* \approx 1.5$. Using low-pass filtered ($\omega \leq \omega_F$) random numbers as the input data, statistics similar to those presented in **Figure 6** were collected for both $\%E_{>\omega=1.5}$ and the artificial dissipation, $adiss$. The quantity $adiss$ is the value of the optimized 10-point artificial dissipation operator whose spectral characteristics are shown in **Figure 8**.

Figure 9 presents the resulting values of $\langle \%E_{>\omega} \rangle_{MEM}$ and $\langle adiss \rangle$ when the bandwidth of the input data varies between $\omega_F = 1.1$ and $\omega_F = \pi$; $\langle \%E_{>\omega} \rangle_{FFT}$ is also indicated for reference. The resulting curve for both $\langle \%E_{>\omega} \rangle_{MEM}$ and $\langle adiss \rangle$ suggests it should be possible to select an appropriate threshold for grid refinement. On a logarithmic scale, the slope characteristics of $\langle adiss \rangle$ are slightly better than those of $\langle \%E_{>\omega} \rangle_{MEM}$. However, an absolute threshold for $adiss$ may be more difficult to define.

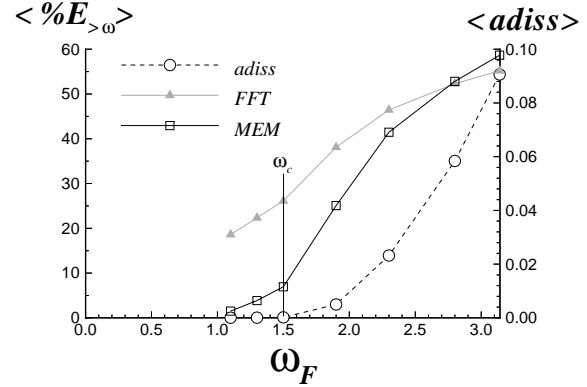


Fig. 9. Mean Percentage of Energy Above $\omega = \omega_c$ as a Function of Asymptotic Input Data Bandwidth ω_F .

5. GRID ADAPTATION RESULTS

Traditional on-the-fly grid adaptation schemes are not based on true error estimates. They are, instead, based on gradients, and the level of error is unknown. By contrast, the candidate methods considered in this study use the energy content of the contravariant fluxes in the Euler or Navier-Stokes equations as a local grid refinement indicator. For a spatial discretization scheme that is accurate up to a wave number $\omega \leq \omega^*$, the presence of energy above ω^* indicates the need for grid refinement. The consequence of grid refinement is to shift the energy in the solution to lower frequencies which are accurately resolved. Conversely, the absence of energy above a wave number $\omega_c < \omega^*$ signals the possibility of coarsening the grid without loss of accuracy.

To test these ideas, we consider the following test problem. Let v_θ denote the tangential velocity for a Lamb vortex:

$$v_\theta = \frac{\Gamma}{2\pi r} (1 - e^{-r^2/4\nu t})$$

where r is the radial distance from the core, Γ is the circulation, t is time, and ν is the kinematic viscosity of the fluid. The Lamb vortex is a solution of the incompressible Navier-Stokes equations representing the decay of an ideal line vortex (Ref. 10). The Lamb vortex model also happens to match reasonably well experimental measurements of tip vortices associated with the flow over helicopter rotor

blades (Ref. 11). In addition to having practical relevance, the Lamb vortex profile provides a challenging case for the evaluation of grid refinement schemes.

Consider a one-dimensional cut $v(x)$ across the Lamb vortex. Suppose the velocity field is to be solved at discrete points on a computational mesh. The unevenly spaced grid is characterized by a mapping $\xi = \xi(x)$ between physical space (x) and computational space (ξ). The grid density ξ_x represents the number of computational points per unit x .

At each point on the computational grid, local MEM spectral estimation is used to obtain the percentage of energy $\%E_{>\omega}$ above a cutoff frequency, ω_c . In this exercise, the percentage of energy is based on a hypothetical flux term $\xi_x v$ (alternatively, $\xi_x v^2$). In the example depicted in **Figures 10** and **11**, we start with a coarse uniform grid ($\Delta x = 80$), resulting in a severely under-resolved vortex profile (grey line in **Figure 11**). The grid refinement scheme assumes the use of a high-order discretization scheme, such that $\omega_c = \omega^* \approx \pi/2$. Each time $\%E_{>\omega}$ exceeds a threshold of 2%, the point is marked for future grid refinement. The grid refinement strategy is a two-step process: (1) multiplication of the local ξ_x by a mesh concentration factor $\gamma > 1$, and (2) integration of ξ_x to produce the new mapping $\xi(x)$. The error estimation/grid refinement sequence is repeated till convergence is attained, i.e., until the condition $\%E_{>\omega} < 2\%$ is everywhere satisfied. The resulting grid density at successive iterations is shown in **Figure 10**. The corresponding grid layout is shown in **Figure 11**.

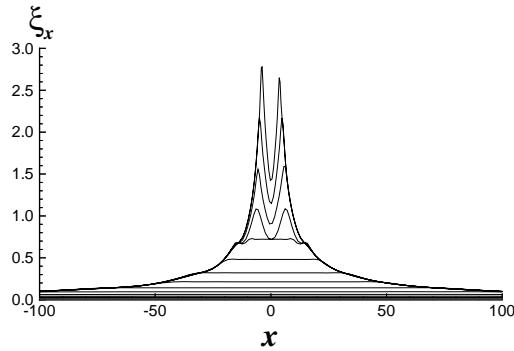


Fig. 10. Grid Density Plot Illustrating the Convergence of the Grid Refinement Procedure for a Lamb Vortex Profile ($\omega_c = \pi/2$, $\%E_{>\omega} < 2\%$).

Note that the method was able to pick on a relatively weak feature of the initial grid (the under-resolved vortex) and *automatically focus in* on the vortex. This is, of course, exactly the quality that is desired in order to detect the type of flow features associated with incipient flow separation.

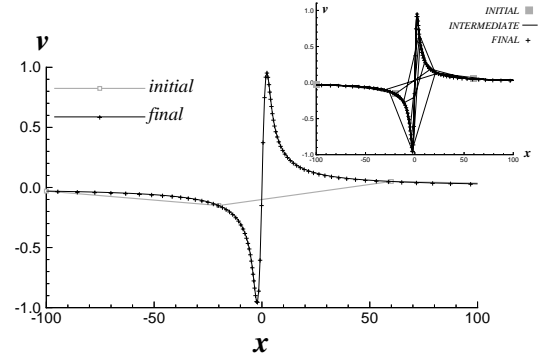


Fig. 11. Evolution of Vortex Profile Resolution Based on Spectral MEM Grid Refinement Strategy ($\omega_c = \pi/2$, $\%E_{>\omega} < 2\%$).

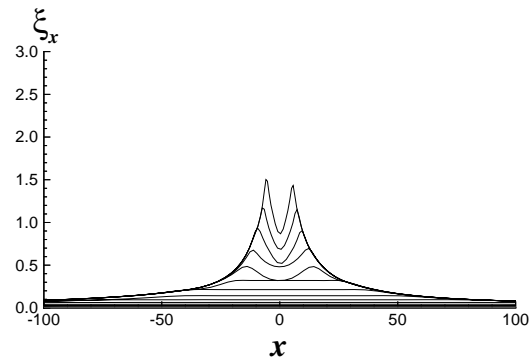


Fig. 12. Grid Density Plot Illustrating the Convergence of the Grid Refinement Procedure for a Lamb Vortex Profile ($\omega_c = \pi/2$, $\%E_{>\omega} < 10\%$).

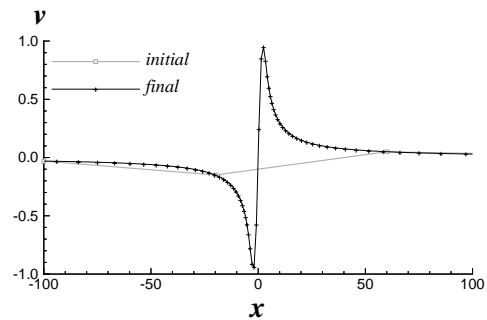


Fig. 13. Evolution of Vortex Profile Resolution Based on Spectral MEM Grid Refinement Strategy ($\omega_c = \pi/2$, $\%E_{>\omega} < 10\%$).

On the other hand, suppose a spatial discretization scheme of lesser accuracy is used, such that $\omega^* \approx \pi/4$ (corresponding, for example, to a fourth-order scheme). Then, for the same energy threshold of 10%, reducing the cutoff frequency from $\omega_c = \pi/2$ (Figures 12 and 13) to $\omega_c = \pi/4$ (Figure 14) produces an increase in the grid density ξ_x and, correspondingly, a larger number of grid points. This, again, is consistent with the expectation that lower accuracy schemes require more grid points in order to accurately resolve the same flow feature.

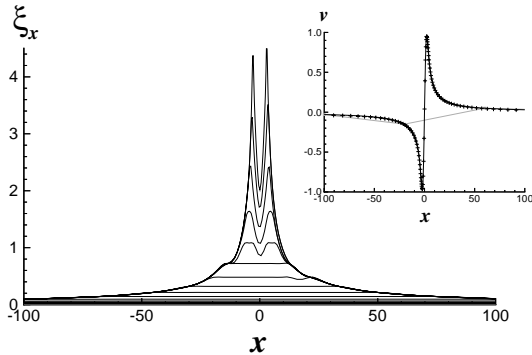


Fig. 14. Evolution of Vortex Profile Resolution Based on Spectral MEM Grid Refinement Strategy ($\omega_c = \pi/4$, $\%E_{>\omega} < 10\%$).

- At this point, we have shown that the method is capable of self-focusing, that the amount of resolution depends on the energy threshold, and that it also depends on the bandwidth of the discretization scheme. Additionally, the spectral-based grid refinement scheme can easily be adapted to any numerical scheme, by appropriately selecting the cutoff frequency ω_c .

As pointed out in the previous section, if the artificial dissipation filter is finely tuned to match the spectral characteristics of the discretization scheme, then the value of the artificial dissipation itself could also be used as an appropriately weighted error estimate. This concept is illustrated in Figure 15, which uses a 10-point optimized artificial dissipation scheme as the driver for mesh refinement. The scheme is applied to the same vortex profile as Figures 10 through 14, and the absolute threshold for grid refinement is set to $adiss < 2 \times 10^{-4}$.

While Figure 15 displays some qualitative similarities with the results presented earlier, the sensitivity to the $adiss$ threshold was found to be greater. In particular, above a certain threshold ($\sim 5 \times 10^{-4}$), no refinement ever took place from the initial coarse grid, while below a certain threshold ($\sim 1 \times 10^{-4}$) the procedure was unstable. Anecdotal evidence

suggests the instability to be caused by the very noise introduced as a result of the grid refinement implementation. Recall that the metric term ξ_x is an integral part of the contravariant flux. Thus, a high frequency content of ξ_x may trigger the grid refinement indicator, even if v or v^2 has low-frequency content. If the indicator threshold is sufficiently sensitive, it is possible for further grid refinement to be triggered purely on the basis of prior grid refinement at that location. This ‘runaway refinement’ could also happen, in principle, with the MEM-based spectral estimation. However, this phenomenon has not been observed in any of our tests. At this point, the conclusion is that, although there are some practical advantages to the use of the *adiss* parameter, the Maximum Entropy method appears to be more robust.

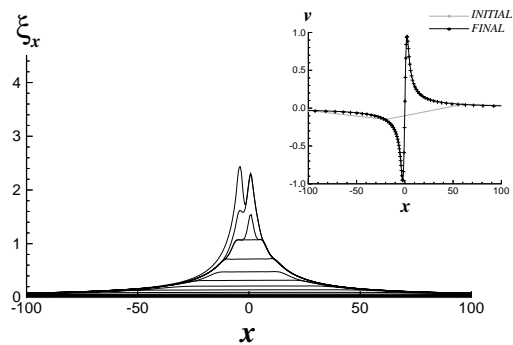


Fig. 15. Evolution of Grid Density and Vortex Profile Resolution Based on Artificial Dissipation Grid Refinement Strategy ($adiss < 2 \times 10^{-4}$).

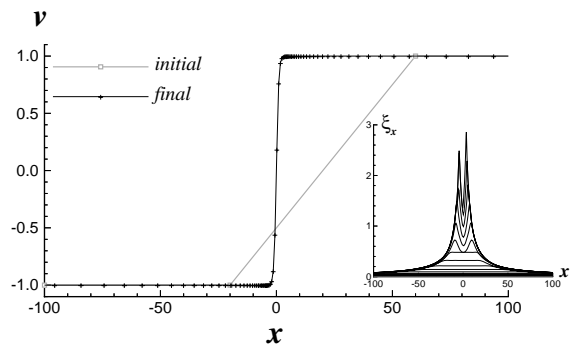


Fig. 16. Evolution of Shear Layer Profile Resolution Based on Spectral MEM Grid Refinement Strategy ($\omega_c = \pi/2$, $\%E_{>\omega} < 2\%$).

Figure 16 is the analog of Figures 10 and 11 in the case of a hyperbolic tangent *shear layer* profile. Again, the initial grid is uniformly coarse, with $\Delta x = 80$. It is hypothesized that a high-order spatial discretization scheme is used, such that $\omega_c = \omega^* \approx \pi/2$. The energy threshold is set to

$\%E_{>\omega} < 2\%$. As in the case of **Figure 11**, the spectral-based grid refinement method is capable of automatically focusing the mesh points on the shear layer. Note also that, generally speaking, ξ_s in the central region (i.e., either the core of the vortex, or the center of the shear layer) is *smaller* than at the edges. This is a consequence of the nearly linear form of the profiles in the core and is, therefore, an indicator of the sensitivity of the method.

Grid Derefinement

The cases presented thus far have considered only the case of grid refinement. Equally important to the success of the method is its ability to *coarsen* or *derefine* the grid, as appropriate. An example of derefinement is given in **Figure 17**. The derefinement method works as follows. At each point on the computational grid, local spectral estimation by the MEM is used to obtain the percentage of energy $\%E_{>\omega}$ above a frequency $\omega_c = \omega^*/\gamma$ (rather than ω^*), where $\gamma > 1$ is a preset relative mesh dilution parameter. In the example depicted in **Figure 17**, the initial grid is one previously obtained by mesh refinement. The subsequent grid derefinement is based on the parameters $\omega_c = \pi/3$ and $\%E_{>\omega} < 0.7\%$.

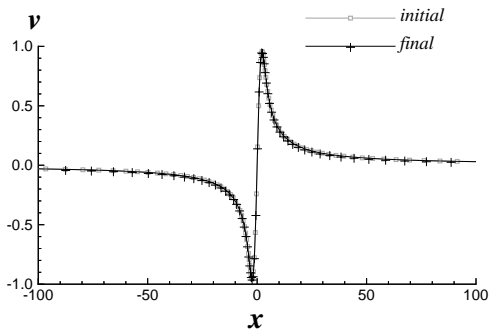


Fig. 17. Evolution of Vortex Profile Resolution Based on Spectral MEM Grid Derefinement Strategy ($\omega_c = \pi/3$, $\%E_{>\omega} < 0.7\%$).

Simultaneous grid refinement and derefinement was also implemented. In this case, both $\%E_{>\omega}(\omega_c = \omega^*)$ and $\%E_{>\omega}(\omega_c = \omega^*/\gamma)$ are constantly monitored. Points are either marked for future refinement or derefinement. The local grid density ξ_s is modified accordingly and integrated to yield the new mapping $\xi(x)$. An example of dynamic refinement / derefinement is given in **Figure 18**. As in **Figure 11**, the initial grid (not shown) is a coarse uniform grid characterized by $\Delta x = 80$. The algorithm parameters are: $\omega^* = \pi/2$, $\gamma = 3/2$, and $\%E_{>\omega} < 2\%$. The vortex is initially centered at $x = 0$. After a fixed number of iterations, the grid focuses on the vortex profile (as in **Figure 11**, but with a greater economy of mesh points, since active derefinement is simultaneously used to optimize point placement). The location of the vortex is then impulsively moved to the right by $\Delta x = 10$. After a

few iterations, the grid point clustering is seen to follow the vortex location as the process continues.

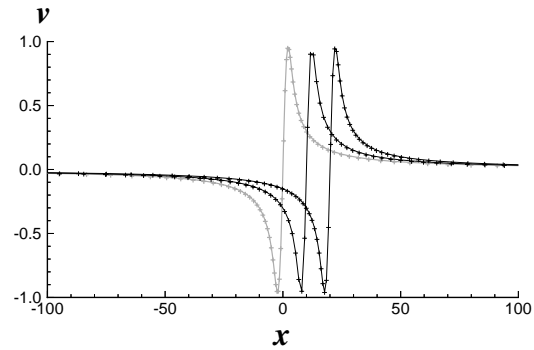


Fig. 18. Illustration of Dynamic Feature-Tracking Using an Impulsively Displaced Vortex. The Simultaneous Grid Refinement/Derefinement Strategy is Based on Spectral MEM.

Note that the results presented in **Figure 10** through **18** are based on the detection of high wave number energy in a ‘model’ contravariant flux, $\xi_s v$. No equations were actually solved in this case: $v(x)$ is a lookup subroutine. Thus, in these examples, there is no feedback resulting from actually solving for the velocity profile on a given computational mesh.

Application to Solutions of Dynamic Stall

The above results demonstrate the value of maximum entropy spectral estimation as a driver for mesh refinement/derefinement. The examples considered were model one-dimensional problems representing profiles typical of generic fluid dynamical entities: vortices and shear layers. In this section, spectral error estimation is applied to nominally well-resolved numerical solutions of dynamical stall.

The solution sets are those obtained in a previous study (Ref. 12) using an eighth-order accurate discretization scheme with eighth-order artificial dissipation on a fine structured curvilinear grid in order to achieve grid independence. The calculations simulated two-dimensional unsteady flow separation about the leading edge of a NACA0012 airfoil at $\alpha = 15^\circ$ angle of attack. The freestream conditions for the cases analyzed here were: $M_\infty = 0.2$ for the Mach number, and $Re = 400,000$ for the chord Reynolds number.

Figure 19 is a snapshot of the dynamically developing vorticity field at $tU/c = 0.090$. Application of the MEM error detection to the streamwise momentum yields contours of the local spectral error in that variable. For example,

Figure 20 depicts contours of streamwise error in ρu . Thus, concentrations of error contours in **Figure 20** are to be interpreted as regions of the solution which are in need of further grid refinement in the streamwise direction. The MEM error contours indicate that the vortices are well-resolved (something the fine computational grid was designed to do). However, further refinement is needed for the fine scale features of the flow, such as secondary and tertiary shear layers developing between the vortices. It is also interesting to notice that grid refinement is suggested for the upstream separating shear layer. This is consistent with the fact that the fixed grid in this case was designed to achieve maximum streamwise resolution between $x/c = 0.013$ and $x/c = 0.047$.

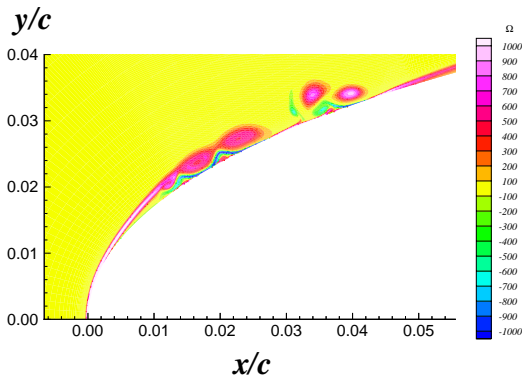


Fig. 19. Instantaneous Vorticity Field at $tU/c = 0.090$, $Re = 400,000$, $\alpha = 15^\circ$.

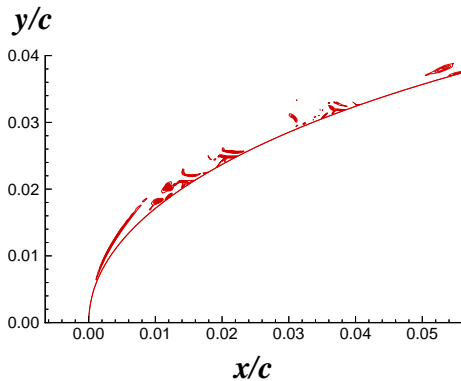


Fig. 20. Contours of Spectral Error Indicating the Need for Streamwise Grid Refinement (Cutoff Frequency: $\omega_{c_0} = \pi/4$).

The MEM spectral error estimator is seen to perform similarly well in **Figure 21**, which corresponds approximately to the time of formation of the primary stall vortex. In **Figure 22**, the boundary layer flow is fully attached, and there is no flow reversal. Yet, the MEM spectral estimator points to a very specific region of the flow near the leading edge as being in need of grid refinement.

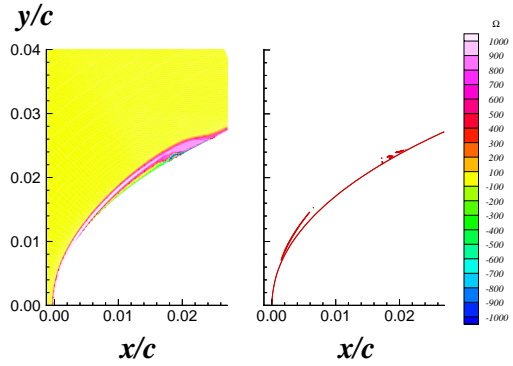


Fig. 21. Comparison of Instantaneous Vorticity Field (Left) and Contours of Spectral Error (Right) Indicating the Need for Streamwise Grid Refinement. ($tU/c = 0.051$.)

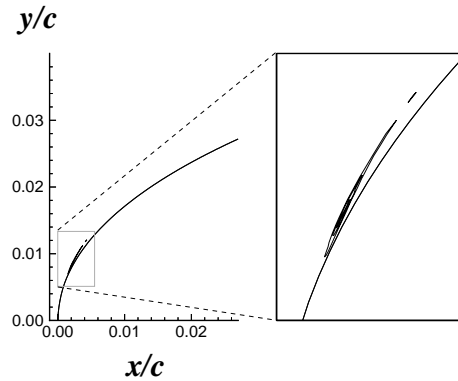


Fig. 22. Spectral Error Contours Indicating the Need for Streamwise Grid Refinement at a Very Early Stage of the Dynamic Stall Process (i.e., *prior* to any flow reversal near the surface; $tU/c = 0.015$).

6. SUMMARY

The ultimate success of a dynamic adaptive flow solver hinges on the development of mesh enrichment indicators which enable the grid refinement to “stay ahead” of a nonlinear solution which is generating finer and finer scales.

This paper describes a novel detection scheme for grid refinement and derefinement, based on the spatially local detection of high wave numbers outside the resolved bandwidth of the CFD algorithm. Spectral estimation is carried out on short data records using the Maximum Entropy method, and one-dimensional examples are shown for a shear layer and a Lamb vortex, both stationary and convecting. The resulting grid resolution is shown to be dependent on an adjustable energy threshold and on the bandwidth of the discretization scheme. Additionally, this

spectral-based grid refinement method can easily be adapted to any numerical scheme, by appropriately selecting the cutoff frequency. Finally, the grid refinement indicator was applied to two-dimensional numerical solutions of dynamic stall. Although these solutions were nominally converged, thin regions of discretization error are indicated at the early stages of flow separation.

The issue of whether or not sufficient grid resolution was applied in the calculations of References 3 and 12 will be reexamined using the new Unstructured MacroCell code presently being developed (Ref. 4).

ACKNOWLEDGMENT

The authors gratefully acknowledge the support of this work by the Army Research Office under Phase I SBIR Contract DAAH04-96-C-0021, monitored by Dr. Thomas L. Doligalski.

REFERENCES

1. Cassel, K.: A Numerical Evaluation of the Theoretical Description of Unsteady Separation, AIAA paper 96-2143, 1996.
2. Choudhuri, P. G. and Knight, D. D.: Effects of Compressibility, Pitch Rate and Reynolds Number on Unsteady Incipient Boundary Layer Separation Over a Pitching Airfoil, AIAA Paper 95-0782, Jan. 1995.
3. Reisenhel, P. H.: Further Results on the Reynolds Number Scaling of Incipient Leading Edge Stall, AIAA Paper 95-0780, Jan. 1995.
4. Childs, R. E., Treidler, E. B., Ekaterinaris, J. A., and Reisenhel, P. H.: A High-Accuracy Solution-Adaptive Unstructured Macro-Cell Algorithm for CFD, AIAA Paper 99-0917, Jan. 1999.
5. Reisenhel, P. H. and Childs, R. E.: Advanced Adaptive CFD Methodology for Dynamic Stall, Nielsen Engineering & Research, NEAR TR 514, Nov. 1996.
6. Childs, R. E. and Reisenhel, P. H.: A Study of Compressible Turbulence, AFOSR TR 96-0288, May 1996.
7. Burg, J. P.: Array Research Analysis of K-Line Wave Number Spectra From the TFO Long Noise Sample, Texas Instruments, Inc. (Science Services Division), Dallas, TX, Feb. 1967.
8. Ulrych, T. J.: "Maximum Entropy Power Spectrum of Truncated Sinusoids," *J. Geophys. Res.*, Vol. 77, No. 8, 1972, pp. 1396-1400.
9. Press, W. H., Teukolsky, S. A., Vetterling, W. T., and Flannery, B. P.: *Numerical Recipes in Fortran*, Cambridge University Press, New York, 1992.
10. Panton, R. L.: *Incompressible Flow*, John Wiley & Sons, New York, 1984.
11. Leishman, J. G. and Bagai, A.: Challenges in Understanding the Vortex Dynamics of Helicopter Rotor Wakes, AIAA Paper 96-1957, Jun. 1996.
12. Reisenhel, P. H.: Vorticity Dynamics and Control of Dynamic Stall, Nielsen Engineering & Research, NEAR TR 482, Aug. 1994.
13. Reisenhel, P. H., Corke, T. C., Koga, D. J., and Nagib, H. M.: Spectral Determination of Unsteady Flow Phenomena by the Maximum-Entropy Method, Proceedings of the AFOSR/FJSRL/U Colorado Workshop on Unsteady Separated Flows, Colorado Springs, CO, Aug. 11, 1983, pp. 123-124.